


# VHE FSRQs with Fermi-LAT: VHE and even brighter states in high-z FSRQs due to an HBL-like component?

MEGHA <sup>1</sup>, PANKAJ KUSHWAHA,<sup>1</sup>  
(AAS JOURNALS DATA EDITORS)

<sup>1</sup>*Department of Physical Sciences, Indian Institute of Science Education and Research (IISER) Mohali  
Knowledge City, Sector 81, SAS Nagar, PO Manauli 140306, India*

## ABSTRACT

Very high-energy (VHE) detected flat-spectrum radio quasars (FSRQs) are relatively few despite being the most persistent bright MeV-GeV sources. Focusing on VHE emission, we investigated the spectral and temporal properties of VHE-detected FSRQs using 14-year Fermi-LAT data. All are highly variable (flux-amplitude>100) with VHE detection associated with brighter flux states and relatively harder spectra. Above a flux limit, flux anti-correlates with spectral index, exhibiting a bluer-when-brighter trend. The low-flux state spectral energy distributions (SEDs) for all resembles a power-law, while high-flux and VHE-associated states resemble a log-parabola, accompanied by an almost nil (PKS0736+017, PKS1510-089) to marginal (4C+21.35, 3C279) to significant (B21420+32, TON0599, PKS1441+25, S30218+35, PKS0346-27, OP313) MeV-GeV peak-upshift – more prominent in high-redshift sources. For no/marginal peak-upshift, the VHE emission is consistent with external Comptonization of infrared photons (EC-IR) driven primarily by a power-law continuation of the particle spectrum to higher energies. For those with a significant MeV-GeV peak-upshift, PKS0346-27 and OP313 shows peak-upshift in the synchrotron spectrum, and thus VHE is EC-IR origin, while for others without synchrotron-peak upshift, we attribute the VHE to an HBL-like component with a Compton-Dominance (CD) like FSRQs, with VHE driven primarily by particle spectrum continuation. In some, even high-state SEDs seem to require an HBL-like component. Thus, VHE activities in FSRQs mainly result from particle spectrum continuation, aided by spectral transition or a new HBL-like component with FSRQ-like CD. Such spectral changes naturally brighten the GeV-VHE flux, overcoming extragalactic background light absorption without requiring extraordinary brightening under the traditional EC-IR scenario than normally exhibited.

## 1. INTRODUCTION

Blazar is an active galactic nuclei (AGN) subclass designated radio-loud that harbors large-scale, powerful bipolar relativistic jets directed almost along the line joining the source and the Earth ( $\leq 15^\circ$ ; Urry & Padovani 1995). It comprises traditionally classified BL Lacertae objects (BL Lacs) and flat-spectrum radio quasars (FSRQs). The traditional classification is based on the strength of optical emission lines with respect to the underlying continuum, which is measured in terms of the equivalent width (EW). In this scheme, BL Lacs have  $EW \leq 5 \text{ \AA}$ , while FSRQs have strong broad emis-

sion lines (Blandford & Rees 1978). The observational traits of blazars are a rapidly variable non-thermal continuum spanning all the accessible EM spectrum from radio up to GeV/TeV gamma-ray energies, high and variable polarization at radio, optical, and even at X-ray in many (Fan et al. 2008; Itoh et al. 2016; Middei et al. 2023), superluminal features in radio images, and intraday variability (Wagner & Witzel 1995).

The spectral hallmark characteristic of a blazar's broadband continuum is its broad bimodal spectral energy distribution (SED; Fossati et al. 1998; Abdo et al. 2010). The lower-energy component extends from radio up to X-rays, peaking at near-infrared (NIR) to X-rays, while the high-energy component extends from X-rays up to TeV, peaking in the MeV-GeV energy bands. One interesting aspect of this bimodal shape

is the frequency at which the low-energy component peaks is exceptionally stable (with few exceptions, e.g., Mkn 501, PKS 1441+25; Pian et al. 1998; Ahnen et al. 2015) despite huge flux variations. Further, the location of this peak anticorrelates with the source luminosity and shows a sequence classification as low-synchrotron-peaked (LSP), intermediate-synchrotron-peaked (ISP), and high-synchrotron-peaked (HSP) (Abdo et al. 2010).

A strong and variable linear polarization at radio, optical, and even X-rays in some and the non-thermal nature of spectra strongly suggest that the low-energy hump is synchrotron emission from the relativistic electrons gyrating in the magnetic field inside the jet. The origin of the high-energy hump is one of the highly debated open issues, and the plausible emission scenarios involve relativistic leptons or hadrons (primarily protons; Böttcher et al. 2013). The hadronic scenario attributes the high-energy hump to either individually or a combination of proton synchrotron radiation and/or proton-proton, proton-photon initiated cascades leading to pion production (Mannheim & Biermann 1992; Mücke & Protheroe 2001). The claim of association of neutrinos from a few blazars supports hadronic processes, while SED modeling suggests an insignificant contribution to MeV-GeV emission, indicating that MeV-GeV emission is primarily due to leptonic processes (Gao et al. 2019; Liodakis & Petropoulou 2020; Acharyya et al. 2023).

The leptonic channel explains the high-energy emission via inverse Compton (IC) scattering (Maraschi et al. 1992; Ghisellini & Tavecchio 2009) since there is an abundance of a wide variety of prominent soft-photon fields, like the broad-line region (BLR; Sikora et al. 1994), IR photons from the dusty torus (Blażejowski et al. 2000), accretion disc (AD; Dermer & Schlickeiser 1992), or cosmic microwave background (CMB) photons (Tavecchio et al. 2000) apart from the synchrotron photons themselves (SSC model; Bloom & Marscher 1996).

FSRQs are strong gamma-ray emitters, with the total radiative budget dominated entirely by the MeV-GeV emission, yet they appear to be weak VHE emitters. So far, only 10 out of 750 *Fermi*-detected FSRQs (Ballet et al. 2024) have been detected at VHE<sup>1</sup>. In the leptonic scenario, FSRQs' MeV-GeV emission is argued to be predominantly due to IC scattering of BLR (IC-BLR) and IR (IC-IR) photon fields. For VHE, IC-BLR is irrelevant due to the Klein-Nishina effect, restricting the output to 20-30 GeV. Further, BLR photons provide strong opacity to the VHE photons through photo pair

**Table 1.** Basic details of the nine VHE-FSRQs considered in this work.

Name	RA	DEC	$z^*$	$F_R$
PKS 0736+017	07 39 17.0	+01 36 12	0.18941 <sup>1</sup>	168
PKS 1510-089	15 12 52.2	-09 06 21.6	0.361 <sup>2</sup>	902
4C +21.35	12 24 54.4	+21 22 46	0.432 <sup>3</sup>	314
3C 279	12 56 11.1	-05 47 22	0.5362 <sup>4</sup>	144
B2 1420+32	14 22 30.38	+32 23 10.44	0.682 <sup>5</sup>	140
TON 0599	11 59 31.8	+29 14 44	0.7247 <sup>6</sup>	106
PKS 1441+25	14 43 56.9	+25 01 44	0.939 <sup>7</sup>	178
S3 0218+35	02 21 05.5	+35 56 14	0.954 <sup>8</sup>	626
PKS 0346-27	03 48 38	-27 49 14	0.991 <sup>9</sup>	134
OP 313**	13 10 28.6638	+32 20 43.783	0.9973 <sup>10</sup>	—

$F_R$  = maximum – flux/minimum – flux  
<sup>1</sup> (Ho & Kim 2009) <sup>2</sup> (Tanner et al. 1996) <sup>3</sup> (Osterbrock & Pogge 1987) <sup>4</sup> (Burbidge & Rosenberg 1965) <sup>5</sup> (Hewett & Wild 2010) <sup>6</sup> (Hewett & Wild 2010) <sup>7</sup> (Shaw et al. 2012) <sup>8</sup> (Cohen et al. 2003) <sup>9</sup> (White et al. 1988) <sup>10</sup> (Schneider et al. 2010)

\*\* We did not consider this source as it was detected at VHE (Nievas Rosillo et al. 2024) after the time duration taken by us.

production, making the BLR opaque to the VHE and implying the emission region to be beyond the BLR (e.g. Böttcher & Els 2016).

The location of the emission region puts a constraint on the predominant soft-photon field for IC scattering. However, observationally, we observe a smooth spectrum that extends well beyond 100 GeV, implying that the very high energy (VHE;  $E > 100$  GeV) is of non-IC-BLR origin. A harder VHE spectrum is observed, which suggests that IC scattering must take place in the Thomson regime. Thus, for VHE emission, a softer photon field is required, and IR photons from the dusty torus are one of the natural and generally favored plausibilities.

In this work, we study the nine<sup>2</sup> VHE FSRQs (see Table 1) to investigate the role of BLR and IR in gamma-ray emission, thus indirectly probing the location of the emission region as well as one-zone or multi-zone emission scenarios. To achieve this, we conducted a comprehensive analysis of the spectral and temporal behavior exhibited by VHE FSRQs during phases of low, high, and VHE gamma-ray activities. The work is organized into five sections. In §2, we discussed the *Fermi* LAT data reduction and the gamma-ray lightcurve and SED analysis procedure. In §3, we present the analysis methods used along with our results, followed by a detailed

<sup>1</sup> <http://tevcat2.uchicago.edu/>

<sup>2</sup> The 10th VHE FSRQ (OP313) was reported in December 2023.

discussion on plausible emission scenarios and the particle spectrum in §4. We conclude in §5.

## 2. FERMI LAT DATA REDUCTION

The *Fermi* observatory was launched on 11 June 2008 with two astronomical payloads onboard: the Gamma-ray Burst Monitor (GBM), primarily for studying gamma-ray bursts, and the Large Area Telescope (LAT), a more sensitive MeV-GeV instrument for surveys. LAT works in the energy range of 20 MeV to >300 GeV with a field of view (FoV) of 2.4 sr. Most of the time, LAT works in ‘scanning mode’, in which it scans the whole sky every 3 hours (Atwood et al. 2009). *Fermi* does not take data while moving over the South Atlantic Anomaly (SAA). On 16 March 2018, a Solar Array Drive Assembly (SADA)<sup>3</sup> anomaly occurred, resulting in a lower exposure for high and low declination sources.

For our sources of interest listed in Table 1 (ascending redshift), we used LAT data between August 2008 and August 2022 and followed the standard data reduction procedures. We performed binned likelihood analysis using *Fermipy* version ‘v1.2’. For our analysis, events belonging to the Source class (evclass=128, evtype=3) and energies between 100 MeV and 800 GeV were used, and a maximum zenith angle cutoff of 90° was applied to reduce the contamination from the Earth’s limb. The analysis was performed with the instrument response function P8R3.SOURCE\_V3, the galactic diffuse emission model (gll\_iem\_v07.fits), and the isotropic background model (iso\_P8R3.SOURCE\_V3.v1.txt) employing the binned maximum likelihood method implemented in the Science tool *gtlike*. The VHE FSRQs are modeled using the default model spectrum as mentioned in the *Fermi* 4FGL catalog (Ballet et al. 2024; Abdollahi et al. 2022), which is either a power law (PL) or a log parabola (LP) with the functional form,

$$PL: \quad \frac{dN}{dE} = N \left( \frac{E}{E_o} \right)^{-\Gamma} \quad (1)$$

$$LP: \quad \frac{dN}{dE} = N \left( \frac{E}{E_o} \right)^{-(\alpha + \beta \log(E/E_o))} \quad (2)$$

where  $dN/dE$  is the differential photon flux in units of  $ph \text{ cm}^{-2} \text{ s}^{-1} \text{ MeV}^{-1}$ ,  $N$  is the normalization factor,  $E_o$  is the scale factor,  $\alpha$  and  $\Gamma$  are the photon indices, and  $\beta$  is the curvature parameter.

Firstly, we extracted monthly binned lightcurves using the *lightcurve* module of *Fermipy*. For this, events with

energies between 0.1 and 800 GeV were selected from an acceptance cone of 15° centered at the location of the source of interest. The model parameters of 4FGL sources within a radius of 10° from the source of interest were left free to vary. Sources with test statistics (TS) >0 and  $n_{pred} > 30$  were chosen for the analysis.

For extracting the SEDs, we used the *SED* module of *Fermipy* in the energy range of 0.1-800 GeV. The number of energy bins was set to 12, and *use\_local\_index* was set to True. SEDs have been generated for the low and high gamma-ray flux states, the VHE activity period, and the entire duration considered in this work.

We used the *Fermipy* flux sensitivity, which provides the value of the minimum photon flux that LAT can detect at a given energy. To further assess the reliability of the extracted SED data points, we calculated sensitivity using the *sensitivity* tool of *Fermipy*. The galactic diffuse model *gll\_iem\_v07.fits* and event class *P8R2.SOURCE\_V6* are used along with a TS threshold of 10.0 and a minimum number of counts of 5.0.

## 3. DATA ANALYSIS AND RESULTS

The monthly photon flux lightcurve extracted by the procedure outlined in §2 for the 9 VHE FSRQs is shown in Figure 1. Data points with TS < 9.0 are plotted as upper limits. The mean of the photon flux and the 3- $\sigma$  band is marked in the light curve with  $\sigma$  defined as the mean of the photon flux error. We used a Bayesian block (Scargle et al. 2013) to mark and identify the photon flux changes (marked by the red solid line). It is a very adaptable and robust statistical method enabling effective identification of significant flux changes. This method segregates the light curve into optimal bins given by  $N$ , which is also mentioned in the figure. The low and high flux states used for SED extraction (§3.3) are marked with gray and cyan shaded regions, respectively. Episodes of VHE detection by ground-based observatories (MAGIC<sup>4</sup>, HESS<sup>5</sup>, and VERITAS<sup>6</sup>) are marked by a purple dashed region.

We found that all the sources are highly variable, with a variation of > 100 times between the maximum and minimum detected photon flux. This ratio is listed in the last column of Table 1, and based on this ratio, the maximum amplitude variation is exhibited by PKS 1510-089 and the minimum by TON 0599 on the monthly time scale. Among these sources, B2 1420+32 and PKS 0346-27 are the ones that remain inactive and below the sensi-

<sup>3</sup> [https://fermi.gsfc.nasa.gov/ssc/observations/types/post\\_anomaly/](https://fermi.gsfc.nasa.gov/ssc/observations/types/post_anomaly/)

<sup>4</sup> <https://magic.mpp.mpg.de/>

<sup>5</sup> <https://www.mpi-hd.mpg.de/hfm/HESS/>

<sup>6</sup> <https://veritas.sao.arizona.edu/>

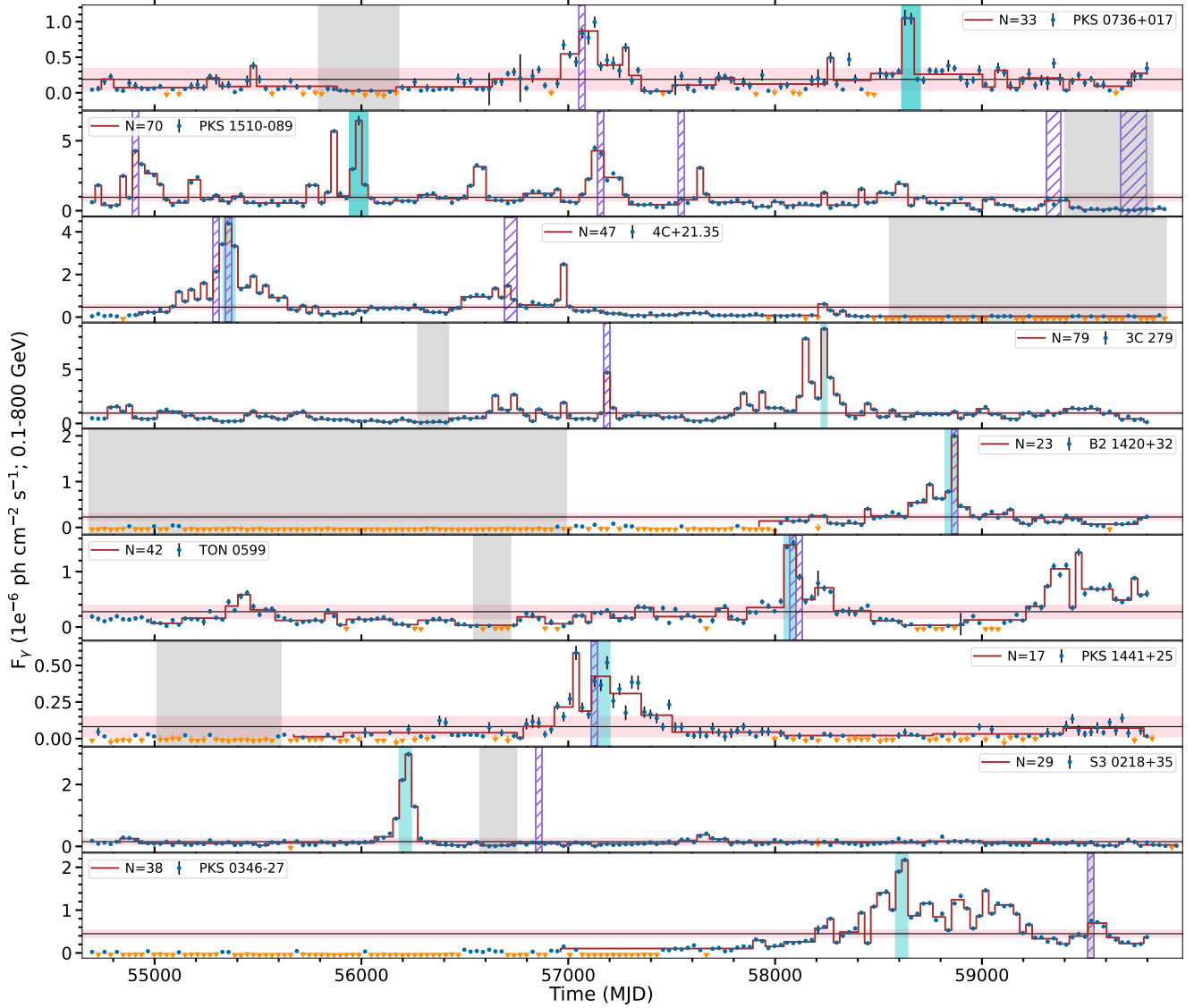


**Figure 1.** Monthly binned light curve of the 9 VHE FSRQs (Table 1) for the duration of 5 August 2008 to August 2022. The *Fermi* data is marked with blue points along with the error bars in black. Orange arrows mark the upper limits ( $TS < 9.0$ ). The Bayesian block is shown in a brown-colored curve, and the number of bins is given by  $N$ . The dashed purple region marks the duration coincident with the VHE detection for which VHE SEDs have been extracted. The horizontal black line is the mean flux with a 3-sigma red color band around the mean. The grey shaded regions mark the duration used for the low flux state SED extraction (ref. §3.3), and the cyan region is used for the high flux state SED. References for VHE detection are: PKS 0736+017 (H. E. S. S. Collaboration et al. 2020), PKS 1510-089 (H. E. S. S. Collaboration et al. 2013; Zacharias et al. 2017; Aharonian et al. 2023), 4C+21.35 (Aleksić et al. 2011; Cerruti 2015), 3C 279 (H. E. S. S. Collaboration et al. 2019), B2 1420+32 (MAGIC Collaboration et al. 2021), TON 0599 (Mirzoyan 2017), PKS 1441+25 (Ahnen et al. 2015), S3 0218+35 (Ahnen et al. 2016), PKS 0346-27 (Wagner et al. 2021).

tivity limit for most of the duration, with the percentage of detection bins being 41% and 51%, respectively.

### 3.1. Histogram

To identify the most observed photon flux state and spectral state at MeV-GeV, we have generated his-

tograms for the logarithm<sup>7</sup> of photon flux (Figure 2 top) and the spectral index (Figure 2 bottom) for all, considering only the detected points. The time of VHE activity is marked with red dotted lines. Histograms were generated employing the Knuth method (Knuth 2013).

<sup>7</sup> to the base 10

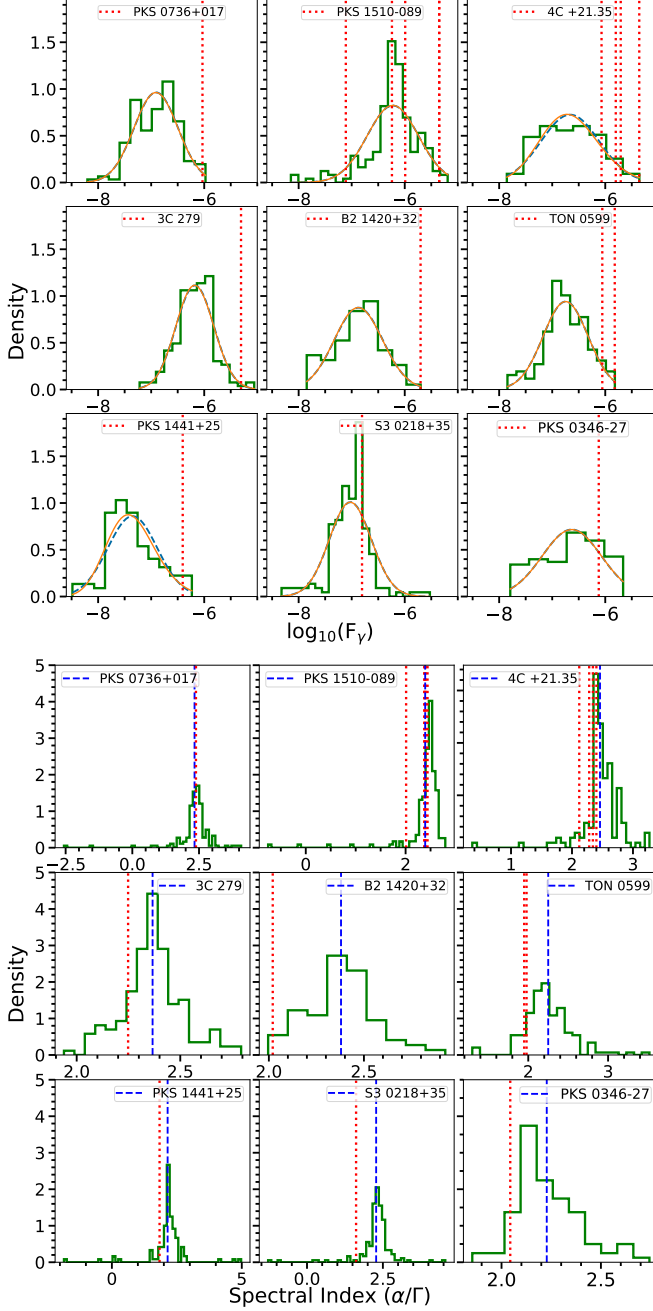


**Figure 2. Top:** Log(flux) histogram plot for all 9 VHE FSRQs with increasing order of redshift from left to right. The solid orange line is a normal fit, and the dashed blue line represents a lognormal fit. The dotted vertical red line represents the value of the log(flux) at the time of the VHE episode. **Bottom:** Spectral index ( $\alpha/\Gamma$ ) histogram plot for all 9 VHE FSRQs with increasing order of redshift from left to right. The dotted red line marks the spectral index at the time of the VHE episode, and the dashed blue line marks the mean spectral index.

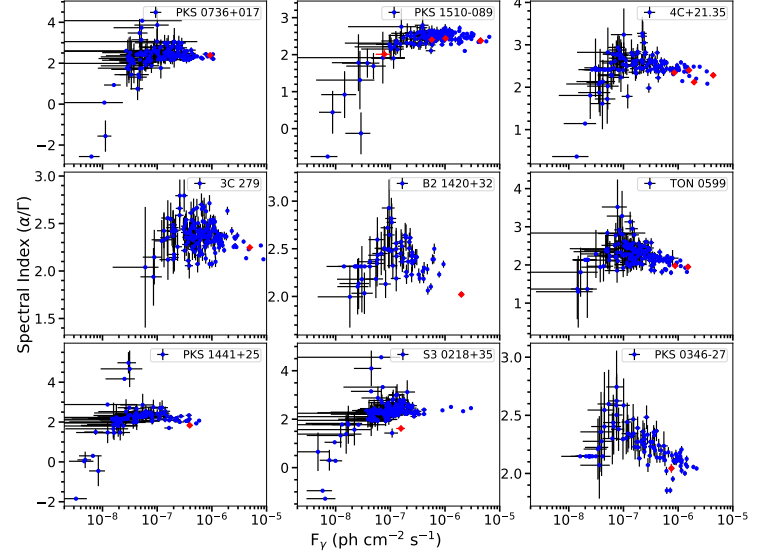


**Figure 3.** Spectral index ( $\alpha/\Gamma$ ) versus flux trend for sources in increasing order of redshift from left to right. Red points mark the MeV-GeV spectral index and photon flux during the time of the VHE episode.

We further tested the histogram of log(photon-flux) with Gaussian and lognormal distributions. We also applied the Kolmogorov-Smirnov (KS) test to assess the goodness-of-fit of the observed log(photon-flux) histogram with both models. The null hypothesis is that there is no significant difference between the data and the normal distribution. For the normal distribution, we obtained the statistics and p-values, respectively, from 0.053 to 0.135 and 0.003 to 0.939. For the lognormal model, we obtained statistics and p-values from 0.053 to 0.100 and 0.061 to 0.933. Based on the p-values, we cannot reject our null hypothesis in general, suggesting that both the normal and lognormal distributions reasonably represent the data well. We observe a continuous distribution of photon flux, and the MeV-GeV spectral indices associated with VHE episodes are between 1.62 and 2.44, in general relatively harder during VHE episodes (Figure 2 bottom panel and Table 2).

### 3.2. Spectral index versus photon flux plots

We also investigated the relation between spectral index and photon flux, and the corresponding plot is shown in Figure 3. The MeV-GeV spectral indices coinciding with the time of VHE activity are represented in red color. Although visual inspection does not indicate any clear pattern or trend, we found a clear trend of bluer-when-brighter (BWB; spectral hardening during brightening) above some flux limit. The lack of any discernible pattern as a whole is likely due to detection in a one/two energy bin during low fluxes and, thus,



a relatively harder spectral index. The flux limits (in  $ph\ cm^{-2}\ s^{-1}$  units) for different sources are: PKS 1510-089 ( $F \gtrsim 1 \times 10^{-6}$ ), 4C+21.35 ( $F \gtrsim 1 \times 10^{-7}$ ), TON 0599 ( $F \gtrsim 1 \times 10^{-7}$ ), PKS 1441+25 ( $F \gtrsim 5 \times 10^{-8}$ ), and PKS 0346-27 ( $F \gtrsim 1 \times 10^{-7}$ ), while for PKS 0736+017 and 3C 279, a slight indication of the trend is seen. For B2 1420+32 and S3 0218+35, no trend is seen. It also clearly shows that VHE detections generally occur during the brighter MeV-GeV flux states and have a relatively harder spectral index (refer to Figure 2).

### 3.3. Low and high flux states SED

Motivated by the association of VHE detection with brighter MeV-GeV flux states, we extracted the MeV-GeV SEDs during high- (no VHE) and low-flux states and also for the time period coinciding with the VHE episodes for a comparative spectral investigation. Various researchers have adopted different criteria for defining low- and high-flux states based on the focus of the study. For example, Meyer & Georganopoulos (2014) adopted a significance-based approach for producing the low-state SED. They have used the method of progressive binning to find the minimum flux based on a chosen TS. Meyer et al. (2019) introduced a more refined way of identifying the low-flux state using light curves extracted using shorter time bins. However, in a photon-starved EM window, such as gamma rays, identifying a few time bins of low-flux states does not yield sufficient count statistics for spectral investigations. Costamante et al. (2018) has used a fixed flux value of  $10^{-6}\ ph\ cm^{-2}\ s^{-1}$ , a value used by the *Fermi*-LAT team to categorize the source as bright<sup>8</sup>.

Our focus is on comparing the different flux state SEDs, which hence requires a good number of photons. Thus, for bright phases, a shorter duration will suffice, so we have chosen the data corresponding to the highest flux only. For low-flux state SED, a longer duration is considered when the source is in low-flux states and/or mostly upper limits, i.e., below the detection limit. This method is broadly similar to Meyer & Georganopoulos (2014), allowing us the extraction of spectra up to and beyond 10 GeV. The SEDs and the best-fit model, along with the  $1-\sigma$  error, are shown in Figure 4, and the parameters are given in Table 2. Again, data points with  $TS < 9.0$  are marked as upper limits. Additionally, we have added the LAT sensitivity curve for each SED, shown by the dotted curves in the respective colors.

## 4. DISCUSSION

**Table 2.** The best-fit spectral parameters for SEDs corresponding to different flux states (refer to §3.3). The spectral parameters with bars ( $\bar{\alpha}$ ,  $\bar{\beta}$ ,  $\bar{\Gamma}$ ) are the mean values estimated from the light curve.

Source Name	State	alpha (LP)	beta
PKS 0736+017 $\bar{\alpha} = 2.33 \pm 0.26$ $\bar{\beta} = 0.46 \pm 0.22$	Low	$2.67 \pm 0.13$	$0.18 \pm 0.12$
	High	$2.38 \pm 0.04$	$0.13 \pm 0.04$
	Full	$2.33 \pm 0.01$	$0.116 \pm 0.009$
	VHE	$2.38 \pm 0.05$	$-0.02 \pm 0.03$
PKS 1510-089 $\bar{\alpha} = 2.39 \pm 0.12$ $\bar{\beta} = 0.07 \pm 0.07$	Low+VHE	$2.18 \pm 0.05$	$-0.02 \pm 0.02$
	High	$2.48 \pm 0.02$	$0.09 \pm 0.01$
	Full	$2.398 \pm 0.004$	$0.059 \pm 0.003$
	VHE	$2.38 \pm 0.02$	$0.04 \pm 0.01$
	VHE	$2.44 \pm 0.05$	$-0.06 \pm 0.23$
4C+21.35 $\bar{\alpha} = 2.46 \pm 0.16$ $\bar{\beta} = 0.14 \pm 0.14$	Low	$2.65 \pm 0.08$	$-0.06 \pm 0.03$
	High	$2.10 \pm 0.01$	$0.079 \pm 0.008$
	Full	$2.303 \pm 0.007$	$0.054 \pm 0.004$
	VHE	$2.12 \pm 0.05$	$0.08 \pm 0.02$
	VHE	$2.28 \pm 0.02$	$0.04 \pm 0.01$
3C 279 $\bar{\alpha} = 2.36 \pm 0.09$ $\bar{\beta} = 0.09 \pm 0.07$	VHE	$2.25 \pm 0.03$	$0.04 \pm 0.02$
	Low	$2.29 \pm 0.09$	$0.06 \pm 0.05$
	High	$2.024 \pm 0.009$	$0.088 \pm 0.006$
	Full	$2.222 \pm 0.004$	$0.082 \pm 0.003$
TON 0599 $\bar{\alpha} = 2.25 \pm 0.18$ $\bar{\beta} = 0.15 \pm 0.14$	VHE	$2.24 \pm 0.02$	$0.06 \pm 0.01$
	Low	$2.32 \pm 0.26$	$0.26 \pm 0.19$
	High	$1.83 \pm 0.02$	$0.079 \pm 0.009$
	Full	$2.071 \pm 0.007$	$0.069 \pm 0.004$
	VHE	$1.95 \pm 0.03$	$0.06 \pm 0.02$
PKS 1441+25 $\bar{\alpha} = 2.14 \pm 0.20$ $\bar{\beta} = 0.28 \pm 0.21$	VHE	$1.98 \pm 0.04$	$0.03 \pm 0.02$
	Low	$2.16 \pm 0.13$	$0.018 \pm 0.06$
	High	$1.89 \pm 0.029$	$0.10 \pm 0.02$
	Full	$2.08 \pm 0.02$	$0.08 \pm 0.01$
S3 0218+35 $\bar{\alpha} = 2.28 \pm 0.21$ $\bar{\beta} = 0.20 \pm 0.16$	VHE	$1.83 \pm 0.06$	$0.13 \pm 0.04$
	Low	$2.09 \pm 0.14$	$0.07 \pm 0.07$
	High	$2.32 \pm 0.02$	$0.12 \pm 0.01$
	Full	$2.27 \pm 0.01$	$0.056 \pm 0.007$
PKS 0346-27 $\bar{\Gamma} = 2.22 \pm 0.09$	VHE	$1.62 \pm 0.11$	$0.05 \pm 0.04$
	Low	$2.42 \pm 0.11$	
	High	$2.02 \pm 0.01$	
	Full	$2.25 \pm 0.01$	
B2 1420+32 $\bar{\Gamma} = 2.38 \pm 0.13$	VHE	$2.02 \pm 0.02$	
	Low	$2.53 \pm 0.09$	
	High	$1.99 \pm 0.01$	
	Full	$2.097 \pm 0.005$	
PKS 0346-27 $\bar{\Gamma} = 2.22 \pm 0.09$	VHE	$2.04 \pm 0.04$	
	VHE		

<sup>8</sup> [https://fermi.gsfc.nasa.gov/ssc/data/access/lat/msl\\_lc/](https://fermi.gsfc.nasa.gov/ssc/data/access/lat/msl_lc/)

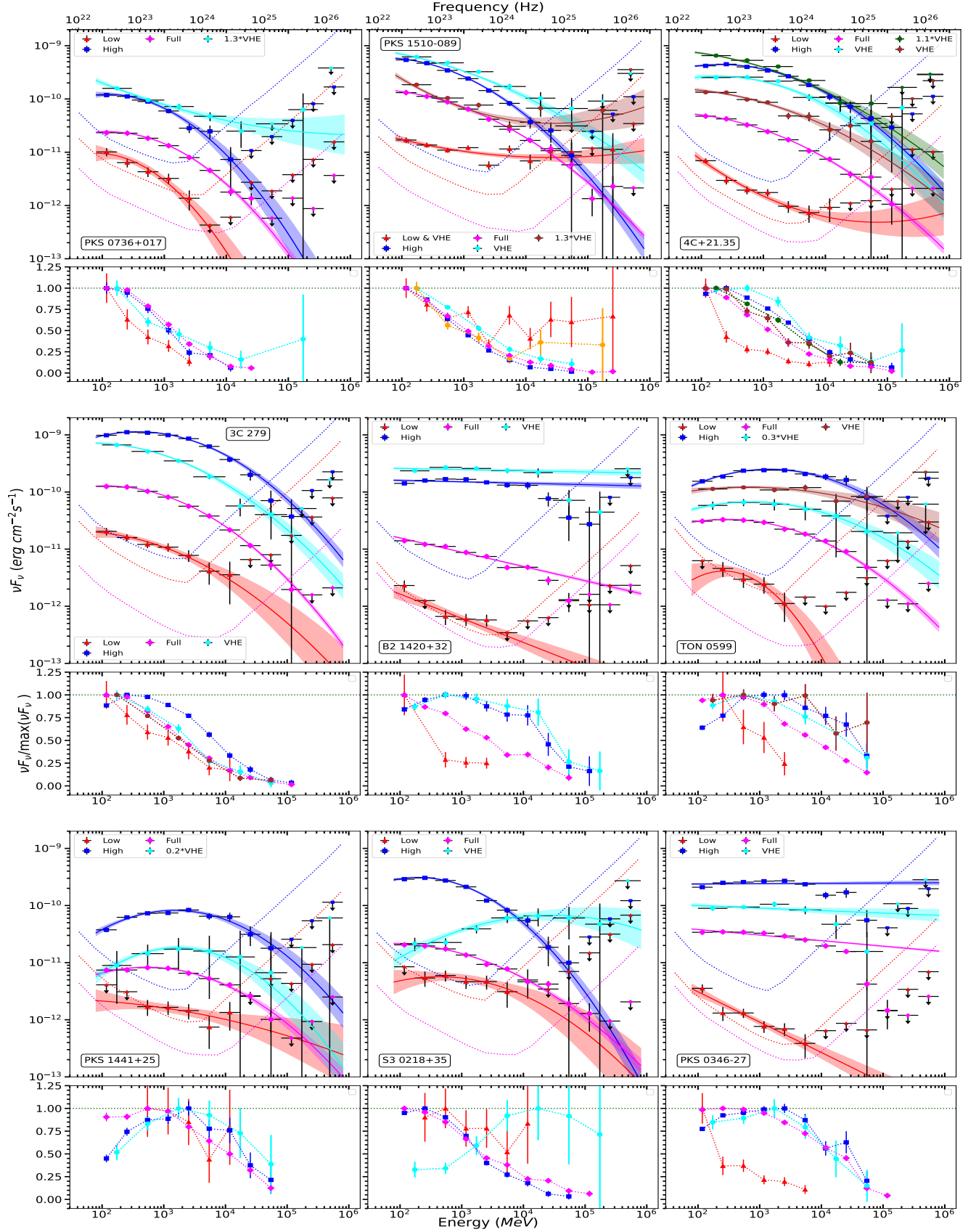


**Figure 4.** MeV-GeV SEDs from LAT for the 9 VHE FSRQs in increasing order of redshift during low (Low) and high (High) flux states, along with the SED for the entire observation period (Full) and VHE detected durations (VHE; see Figure §1). The black arrows mark the upper limits, with dotted curves showing the Fermi-LAT sensitivity for the corresponding states (§2). The numerical factor in the ‘VHE’ label is a scaling factor for a clearer representation. The solid curves are the best-fit model (PL/LP; see Table 2) with a  $1\text{-}\sigma$  shaded region. The lower panel of the SEDs gives the ratio of  $\nu F_\nu$  to  $\max(\nu F_\nu)$ , a good proxy for measuring peak shifts. The dotted horizontal line marks the value of 1.0.

We analyzed the Fermi-LAT data of the VHE-detected FSRQs with a focus on the comparative investigation of MeV-GeV spectral and temporal behavior associated with the VHE activity periods to that of non-VHE. The analysis of the monthly binned light curve (ref. Figure 1) shows that all the VHE FSRQs are highly variable, with the ratio of maximum and minimum photon flux being  $> 100$ . Among all sources, PKS 1510-089 exhibits the highest, while TON 0599 exhibits the least variation in the flux amplitude (Table 1). Since *Fermi* continuously and unbiasedly surveys the sky, the number of Bayesian states can be used as a proxy for measuring the source activity, i.e., a greater number of Bayesian bins implies a more active source. Based on this criterion, 3C 279 and PKS 1510-089 are the most active, while PKS 1441+25 is the least active. Also, B2 1420+32 and PKS 0346-27 remain mostly dormant — quiescent/below sensitivity continuously for most of the time ( $\sim 10$  years).

The photon-flux histograms in Figure 2 are, in general, consistent with both lognormal and normal distributions, though, for a few, one of these seems preferable ( $p=0.05$ ). Similar conclusions have previously been reported using similar time-bin data (e.g., Shah et al. 2018; Wang et al. 2023) for a larger sample with a general preference for log-normal. Shorter time-bins incite more complexity (e.g., PKS 2155-304, PKS 1510-089; H. E. S. S. Collaboration et al. 2010; Kushwaha et al. 2016, 2017).

The VHE emission/activity is generally associated with bright MeV-GeV flux states and has a relatively harder spectrum ( $\alpha/\Gamma$ : 1.6 – 2.44) compared to the non-VHE brighter states ( $\alpha/\Gamma$ : 2.14 – 2.46). The following spectral trend is apparent:

- The MeV-GeV flux is anti-correlated with the spectral index, exhibiting a “bluer-when-brighter” trend above a flux limit (Fig. 3 & §3.2).
- Focusing on a particular source, the high flux spectrum is harder in all except PKS 1510-089 and S3 0218+35 (ref. Table 2).
- As a whole, the limited sample indicates that the spectral parameter,  $\alpha$  ( $\Gamma$ ), is systematically lower (a harder spectrum) for high-redshift FSRQs under the assumed spectral model.

Within the exposure limit and LAT sensitivity, there appears to be a characteristic difference in the spectral shapes, as seen in Fig. 4 (bottom panel of each source). The low-state SED is steeper (except for PKS 1510-089, S3 0218+35, and possibly PKS 1441+25), all resembling a power law, implying the high-energy hump peak at  $\lesssim 300$  MeV. High-state SEDs, on the other

hand, resemble a log parabola with flux in each spectral bin an order of magnitude higher compared to the low state, except for PKS 1501-089. Examining the subplots in Figure 4 that shows the ratio of SED data points with respect to maximum SED value (for detected bins only), we found the high-energy peak shows no (e.g., PKS 0736+017 and PKS 1510-089) to a marginal (e.g., 4C+21.35, 3C 279, and S3 0218+35) to a significant (e.g., B2 1420+32, TON 0599, PKS 1441+25, and PKS 0346-27) upshift ( $\sim 1 - 20$  GeV) during high-state compared to the low-state SED. The shift is more prominent in higher redshift FSRQs. Such shifts have been reported in some of the VHE FSRQs earlier (e.g., PKS 1441+25, PKS 0736+017, and B2 1420+32; Ahnen et al. 2015; Abeysekara et al. 2015; Angioni et al. 2019; Acciari et al. 2021) and also in blazars of other spectral classes (e.g., Mkn 501, 1ES 1215+303, BL Lac; Pian et al. 1998; Valverde et al. 2020; Agarwal et al. 2023). Overall, the average spectrum for the entire duration is biased towards the higher flux-state spectrum, as expected.

Apart from the SED trend stated above, the VHE-associated MeV-GeV SEDs also show some interesting trends compared to the low- and high-state SEDs.

- The VHE-associated MeV-GeV SED is similar to the low state for PKS 0736+017, PKS 1510-089, 4C+21.35, and 3C 279.
- It resembles the high-state SED for B2 1420+32, TON 0599, PKS 1441+25 and PKS 0346-27.
- The VHE-associated MeV-GeV SED of S3 0218+35 has a completely different spectral shape, more like an extreme HBL source.

These observed spectral changes during the different flux states have strong implications for underlying emission processes and the particle spectrum. Since FSRQs are LSP sources and MeV-GeV emission is almost entirely of leptonic origin via IC, also supported by SED modeling of candidate neutrino blazars (e.g., Gao et al. 2019), the observed spectral changes/peak upshift can be primarily due to three reasons:

- (a) A change in the underlying particle spectrum.
- (b) A change of the dominant seed photon field (indirectly the location of the emission region).
- (c) A new additional broadband emission component.

Below, we examine the role of seed photons on the spectral shape, thereby examining its indirect implication to the location of the emission region in the jet.



#### 4.1. Emission scenarios

For FSRQs, IC-BLR and IC-IR are the most argued scenarios for producing MeV-GeV emissions (e.g., MAGIC Collaboration et al. 2018). However, KN disfavors IC-BLR for VHE, and thus only IC-IR (or a strong field with energy  $\lesssim$  IR) is relevant. Further, BLR provides strong opacity for  $\gamma\gamma$  pair production (e.g. Böttcher & Els 2016) and thus, for VHE production, the emission region is generally argued to be outside the BLR.

The emission may also possibly be from two/multiple emission regions. Since the high-state SED is almost an order of magnitude higher than the low-state SED for each source, for all practical purposes, the high-state emission can be considered effectively from a single emission region. For the one-zone scenario, the peak shift reported for the high states is plausible by the IC process through the change in the dominant seed-photon field, indirectly related to the location of the emission region, as demonstrated below.

##### 4.1.1. Location of emission region and gamma-ray spectrum

For IC scattering in the Thomson regime, the total power output depends on the energy density of the seed radiation field.

$$P(\gamma) = \frac{4}{3} \sigma_T c \beta^2 \gamma^2 U_R \quad (3)$$

where  $\sigma_T$  is the Thomson scattering cross section,  $\beta$  is the speed of the particle in units of the speed of light,  $\gamma$  is the particle Lorentz factor, and  $U_R$  is the seed photon field energy density. The two most argued cases for the location of the emission region are: within the BLR or outside the BLR.

**Within BLR:** In this case, both BLR (sub-parsec scale; e.g. Gravity Collaboration et al. 2018) and IR photons (parsec scale; e.g. Jaffe et al. 2004) will be boosted in the blob/emission-region frame (primed quantities), and the respective peak frequencies are given by (e.g., Sahayanathan & Godambe 2012)

$$\nu^P = \left( \frac{\delta}{1+z} \right) \gamma_b'^2 (\Gamma \nu^*) \quad (4)$$

Thus, for typical SED parameters, the observed IR peak ( $T^* = 1200$  K, Malmrose et al. 2011)<sup>9</sup> is

$$\nu_{IR}^P \approx 2.62 \times 10^{21} \left( \frac{\delta}{23.67} \right) \left( \frac{\gamma_b'}{340} \right)^2 \left( \frac{\Gamma}{20.9} \right) \left( \frac{\nu_{IR}^*}{7.05 \times 10^{13}} \right) Hz \quad (5)$$

<sup>9</sup>  $h\nu^* = 2.82 k_B T^*$

and for BLR ( $\text{Ly-}\alpha$ ;  $\nu^* = 2.47 \times 10^{15} Hz$ ), it is

$$\nu_{BLR}^P \approx 9.20 \times 10^{22} \left( \frac{\delta}{23.67} \right) \left( \frac{\gamma_b'}{340} \right)^2 \left( \frac{\Gamma}{20.9} \right) \left( \frac{\nu_{BLR}^*}{2.47 \times 10^{15}} \right) Hz \quad (6)$$

where  $\Gamma$  is the bulk Lorentz factor of the emission region,  $z$  is the source redshift, and  $\gamma_b'$  is the break Lorentz factor of the broken power-law electron distribution used in the SED modeling (e.g. Roy et al. 2021), and  $\delta$  is the Doppler factor,  $\nu_{IR}^*$  ( $T^*$ ) and  $\nu_{BLR}^*$  are respectively the characteristic frequencies of IR and BLR photon fields (assumed thermal) in the AGN frame. Thus, the IC-BLR peak will be at higher frequencies than the IC-IR.

For a given set of parameters, the radiative power output depends only on the energy density of the seed photons (eq. 3). Thus, depending on the relative energy densities of the IR ( $U_{IR}$ ) and BLR ( $U_{BLR}$ ) fields, the MeV-GeV spectrum can exhibit a wide range of SED shapes, like flat, rising, and declining, accompanied by a peak shift. The ratio of their energy density is

$$\frac{U_{BLR}}{U_{IR}} = \frac{f_{BLR}}{f_{IR}} * \left( \frac{T_{BLR}}{T_{IR}} \right)^4 \quad (7)$$

where  $f_{IR}$  and  $f_{BLR}$  are the overall normalization factors, accounting for the unknown factors like geometry, filling factor, covering fraction, etc. So, we present four cases<sup>10</sup>, to demonstrate the effect of varying the energy density of BLR with respect to IR (IR is most relevant for VHE). This is demonstrated in Figure 5 from case (a) to (d) for the SED of 3C 279 for different  $U_R$  using the spectral parameters from Roy et al. (2021).

(a)  $U_{IR} = U_{BLR}$ , i.e., a similar contribution by both except BLR has an early KN onset and, thus, roughly a flat SED in the sub-GeV to GeV range, followed by a spectrum governed by EC-IR at VHE, if the spectrum continues. This is shown in Fig. 5(a).

(b)  $U_{BLR} = 0.1 * U_{IR}$ , improbable in the standard AGN paradigm; can be possible because of the f-factor (clumpy, non-isotropic with the subtended solid angle less than the IR-torus, etc.) and the resulting spectrum is primarily due to EC-IR and peaks at lower energy ( $\sim 100$  MeV; Fig. 5(b)).

(c)  $U_{BLR} = 10 * U_{IR}$ , the output is dominated by BLR, leading to a rising spectral shape, peaking at higher energies ( $\sim 1$  GeV; refer to Fig. 5 (c)). Such SED changes have been seen earlier, e.g., Hayashida et al. (2015).

(d) **Outside BLR but within IR torus:** IR photon density will be boosted, while BLR photons will be

<sup>10</sup> arbitrarily chosen for demonstration only at the moment, but can be used with telescope sensitivity and observed spectral shape to get better constraints

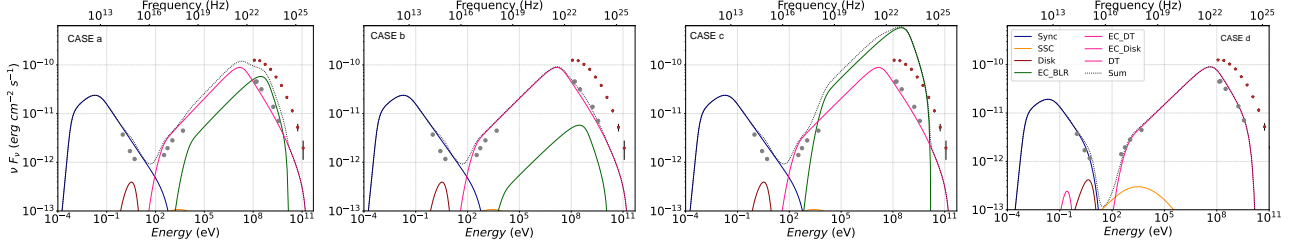


**Figure 5.** Modeled SED for FSRQ 3C 279 demonstrates four different scenarios based on the location of the emission region (ref 4.1.1). The first three figures correspond to cases (a) to (c) detailed in §4.1.1, where the emission region is within the BLR. The fourth figure depicts the case (d) when the emission region lies outside the BLR. Grey points represent the data points from Roy et al. (2021), while red data points represent the average spectra for the entire duration. The dark blue, dark green, deep pink, dark red, and dark orange lines indicate synchrotron EC-BLR, EC-IR (EC-DT), disk thermal, and SSC components, respectively. The dashed black line represents the total spectrum.

deboosted. The respective peak frequencies are

$$\nu_{BLR}^{P,out} = \left( \frac{\delta}{1+z} \right) \gamma_b^2 \left( \frac{\nu_{BLR}^*}{\Gamma} \right) \quad (8)$$

$$\nu_{BLR}^{P,out} \approx 2.10 \times 10^{20} \left( \frac{\delta}{23.67} \right) \left( \frac{\gamma_b}{340} \right)^2 \left( \frac{20.9}{\Gamma} \right) \left( \frac{\nu_{BLR}^*}{2.47 \times 10^{15}} \right) H_z \quad (9)$$

In this case, due to deboosting, BLR will peak at lower energies than IR, and the energy density of BLR will also be lower by a factor of  $\Gamma^2$ . This case has been shown in figure 5 (d).

In the above demonstrated scenarios, both the IR and BLR fields are in the AGN frame, with the IR field temperature already on the higher side, while the BLR field is Ly- $\alpha$ . Thus, FSRQ's MeV-GeV spectrum in the single emission region scenario is shaped by  $U_{IR}$  and  $U_{BLR}$ , dictated by the location of the emission region. Following the demonstration above, the competitive dominance between the two, even without any upshift in the optical-IR synchrotron peak, can lead to a high-energy peak shift if EC-BLR dominates over EC-IR (e.g. Hayashida et al. 2015), the latter being generally the preferred scenario in LSPs for MeV-GeV gamma-rays (low-state SEDs in Figure 4) and VHE emission. However, EC-BLR dominance (emission region within BLR) is ineffective for VHE due to the KN effect, while VHE, which could result from the EC-IR in this case, gets absorbed due to the high opacity of the BLR field through the  $\gamma\gamma$  pair creation channel (Böttcher & Els 2016; Yadav & Kushwaha 2024). Therefore, the VHE is due to EC-IR.

Further, FSRQs' non-thermal optical-IR synchrotron in FSRQs is steeper/softer/declining, and thus, following the trends in Figure 5, the sub-GeV to GeV spectrum should be similar, i.e., steeper/declining if EC-IR dominates with a peak  $\lesssim 100$  MeV (cases (b) and (d)); flatter up to  $\sim 10 - 20$  GeV if EC-BLR and EC-IR have a similar contribution (case (a)); or harder with a

peak shift to around 10-20 GeV in EC-BLR domination (case (c)). If similar considerations hold regardless of the source redshift, the MeV-GeV peak of high-redshift FSRQs should be systematically at lower energies compared to the low- $z$  counterparts.

From the low, high, and VHE-associated SEDs in Figure 4, we have two sets of sources: FSRQs with nil or marginal peak upshift and spectral hardening (Nil: PKS 0736+017, PKS 1510-089; Marginal: 4C+21.35, 3C 279) and FSRQs with substantial peak upshift and hardening (B2 1420+32, TON 0599, PKS 1441+25<sup>11</sup>, S3 0218+35, PKS 0346-27). Noting that IR and BLR seed photons are in the AGN frame, a significant upshift is possible only due to either a significant upshift of the low-energy peak, i.e., the optical-UV synchrotron peak, or a new emission component (§4.1).

For FSRQs with no/marginal peak upshift – all low-redshift ones, multi-wavelength observations during high-flux and VHE episodes do not indicate significant upshift of the synchrotron peak (e.g., Ahnen et al. 2015; Acciari et al. 2021; Aharonian et al. 2023; H. E. S. S. Collaboration et al. 2019). Thus, both the VHE and the high-energy emission are due to EC-IR, as normally argued. However, the spectral hardening seen during VHE as well as in the high states (harder than the VHE spectrum) implies that the VHE emission is primarily a result of a power law extension of the high-energy end of the underlying particle spectrum, i.e., the optical-UV synchrotron spectrum extends to X-ray energies (e.g., MAGIC Collaboration et al. 2018; Aharonian et al. 2023).

For FSRQs exhibiting a significant peak upshift (high-redshift ones), the VHE emission can be explained using the normally argued EC-IR scenario if the IR-optical synchrotron peak shows a similar order peak upshift as

<sup>11</sup> a bit ambiguous due to non-detection at lower energy during the low state.

in the case of PKS 0346-27 (Angioni et al. 2019) and OP 313 (Pandey et al. 2024). For TON 0599, PKS 1441+25, and S3 0218+35, no peak shift in the synchrotron spectrum is reported, and thus we argue that VHE emission is due to an additional HBL/HSP component, which has a Compton dominance (CD) of FSRQ ( $CD \gg 1$ ), contrary to the trend inferred from the blazar spectral sequence ( $CD \lesssim 1$ ; Fossati et al. 1998; Ghisellini et al. 2017). For B2 1420+32, it is a combination of both cases: the SEDs reported by MAGIC Collaboration et al. (2021) show a significant upshift in the IR/optical spectrum, while the VHE state spectrum shows the need for an additional HBL-like component. The need for an HBL/HSP-like component has already been argued for VHE emission in some of the FSRQs (e.g., PKS 1441+25, S3 0218+35; Ahnen et al. 2015, 2016) and even VHE BL Lacs (e.g., OJ 287; Kushwaha et al. 2018, 2021; Acharyya et al. 2024). In both cases, the CD of the required new HBL-like component is that of the respective spectral class, indicating that CD is intrinsic.

Though VHE is associated with brighter MeV-GeV flux states, many (TON 0599, B2 1420+32, PKS 0346-27) have brighter MeV-GeV states and even a harder spectrum compared to the VHE-associated states, but lack VHE association. We argue that the high-state emission in these sources may also be due to an HBL/HSP-like component. For example, for TON 0599, Maurya et al. (2025) reported a requirement of a thermal accretion-disk component, arguing a signature of disc-jet coupling, to fit the low-energy X-ray spectrum from XMM-Newton, while the MeV-GeV emission is explained via EC-BLR and EC-IR. However, a careful examination of the SEDs shows that the model systematically fails to reproduce the highest MeV-GeV fluxes and also that the authors have not used the XMM-Newton spectra in SED modeling. We argue that the claimed thermal component is actually an HBL/HSP component, manifesting as a thermal-like component because of the limited spectral range. A similar issue can be seen in the SED modeling work of Manzoor et al. (2024). Thus, even high-flux states SED could be due to an additional HBL-like component, without VHE association, simply because of the particle spectrum. This indicates that a more nuanced look is required during SED modeling.

From the above discussion, it is possible that if the high-energy particle spectrum giving optical-UV synchrotron continued into X-rays (e.g. Dathan & Kushwaha 2025; Kushwaha 2025), more FSRQs will be candidate VHE sources via the traditional EC-IR scenario. However, increased redshift implies increased EBL ab-

sorption, which requires extraordinary brightening under the EC-IR scenario than what is observed to be detected at VHE. On the contrary, a spectral transition or a new HBL/HSP-spectral component with CD-like FSRQs, though rare, naturally enhances the GeV-VHE flux to negate EBL absorption. For example, the high redshift of the brightest blazar, 3C 454.3, could be a reason for the lack of VHE detection despite intense flaring behavior (e.g., Anderhub et al. 2009).

Thus, in short, VHE in FSRQs is primarily driven by the particle spectrum, combined with spectral transition or a new HBL-like component with the CD of FSRQs in high-redshifted ones. Even high-state MeV-GeV without VHE association in a few could be due to an HBL-like component. It should be noted that recent and previous studies have studied VHE FSRQs, e.g. Malik et al. (2025), explored VHE FSRQs with a focus on the statistical properties of flux and spectral index or SED modeling of limited samples, while we focused on comparative SED shapes and their evolution during low, high, and VHE-associated states.

## 5. SUMMARY AND CONCLUSION

VHE-detected FSRQs are relatively few, and therefore, to unravel and understand VHE and high-energy emission, we systematically studied the spectral and temporal properties of the VHE-FSRQs using 14 years of *Fermi*-LAT data through monthly binned light curves, exploring statistical properties of flux and spectra and SEDs during different flux states. A summary of our results and inferences is as follows:

- All sources are highly variable, with a maximum-to-minimum flux ratio  $> 100$  in monthly bins. PKS 1510-089 is the most variable, and TON 0599 is the least variable, based on the Bayesian block.
- VHE is associated with a brighter MeV-GeV state and, in general, has a relatively harder spectral index. For many, there are brighter MeV-GeV states without VHE.
- The logarithmic-flux histograms are consistent with both normal and lognormal distributions, although a few prefer one of the two.
- Above a flux threshold, the flux anticorrelates with the spectral index, indicating a bluer-when-brighter trend. The lack of this trend at lower flux states is likely due to the detection of fewer photons in a very limited LAT energy range.
- MeV-GeV SEDs during low states resemble PL, whereas the brighter and VHE-associated SEDs

resemble LP. Interestingly, the high-flux state and the VHE SEDs show no (PKS 0736+017, PKS 1510-089), marginal (4C+21.35, 3C 279), or significant peak upshift (B2 1420+32, TON 0599, PKS 1441+25, S3 0218+35, PKS 0346-27, OP 313) compared to the low state. The peak upshift is more prominent in high-redshift sources.

- FSRQs with no/marginal peak upshift (all low redshift ones; PKS 0736+017, PKS 1510-089, 4C+21.35, and 3C 279), the low, high, and VHE emission is due to EC-IR with VHE driven by the extension of the high-energy part of the particle spectrum to higher energies. The same is true for FSRQs (PKS 0346-27 and OP 313), where the synchrotron peak has upshifted by a similar order.
- For FSRQs with a significant MeV-GeV peak upshift (all high redshift ones; TON 0599, PKS 1441+25, S3 0218+35, PKS 0346-27, OP 313) but no upshift of the synchrotron peak, VHE emis-

sion is due to an (extreme) HBL/HSP-like component with a CD of FSRQs (i.e.,  $CD \gg 1$ ), unlike the HBL/HSP CD seen in the blazar sequence ( $CD \lesssim 1$ ), powered by an extension of the high-energy end of the particle spectrum to higher energies. For B2 1420+32, it is a combination of both cases.

- In high- $z$  FSRQs, even high-flux state SEDs could be from an additional HBL-like component.

In a nutshell, VHE is primarily due to a (likely) PL continuation of the high-energy end of the particle spectrum to higher energies supplemented by a spectral transition or a new-jet component with an FSRQ-like CD for high- $z$  FSRQs. The latter may be true even for the high-flux state emission (e.g., TON 0599). For high- $z$  FSRQs, spectral changes naturally boost GeV-VHE flux, negating EBL absorption, which otherwise requires significantly more drastic flux variation than typically seen ( $\sim 100$ ) in the traditional EC-IR scenario.

## APPENDIX

## REFERENCES

- Abdo, A. A., Ackermann, M., Agudo, I., et al. 2010, *ApJ*, 716, 30, doi: [10.1088/0004-637X/716/1/30](https://doi.org/10.1088/0004-637X/716/1/30)
- Abdollahi, S., Acero, F., Baldini, L., et al. 2022, *The Astrophysical Journal Supplement Series*, 260, 53, doi: [10.3847/1538-4365/ac6751](https://doi.org/10.3847/1538-4365/ac6751)
- Abeysekara, A. U., Archambault, S., Archer, A., et al. 2015, *ApJL*, 815, L22, doi: [10.1088/2041-8205/815/2/L22](https://doi.org/10.1088/2041-8205/815/2/L22)
- Acciari, V. A., Ansoldi, S., Antonelli, L. A., et al. 2021, *Astronomy & Astrophysics*, 647, A163, doi: [10.1051/0004-6361/202039687](https://doi.org/10.1051/0004-6361/202039687)
- Acharyya, A., Adams, C. B., Archer, A., et al. 2023, *The Astrophysical Journal*, 954, 70, doi: [10.3847/1538-4357/ace327](https://doi.org/10.3847/1538-4357/ace327)
- Acharyya, A., Adams, C. B., Archer, A., et al. 2024, *ApJ*, 973, 134, doi: [10.3847/1538-4357/ad64d0](https://doi.org/10.3847/1538-4357/ad64d0)
- Agarwal, S., Banerjee, B., Shukla, A., et al. 2023, *MNRAS*, 521, L53, doi: [10.1093/mnras/rlad023](https://doi.org/10.1093/mnras/rlad023)
- Aharonian, F., Benkhali, F. A., Aschersleben, J., et al. 2023, *The Astrophysical Journal Letters*, 952, L38, doi: [10.3847/2041-8213/ace3c0](https://doi.org/10.3847/2041-8213/ace3c0)
- Ahnen, M. L., Ansoldi, S., Antonelli, L. A., et al. 2015, *ApJL*, 815, L23, doi: [10.1088/2041-8205/815/2/L23](https://doi.org/10.1088/2041-8205/815/2/L23)
- . 2016, *A&A*, 595, A98, doi: [10.1051/0004-6361/201629461](https://doi.org/10.1051/0004-6361/201629461)
- Aleksić, J., Antonelli, L. A., Antoranz, P., et al. 2011, *ApJL*, 730, L8, doi: [10.1088/2041-8205/730/1/L8](https://doi.org/10.1088/2041-8205/730/1/L8)
- Anderhub, H., Antonelli, L. A., Antoranz, P., et al. 2009, *A&A*, 498, 83, doi: [10.1051/0004-6361/200811326](https://doi.org/10.1051/0004-6361/200811326)
- Angioni, R., Nesci, R., Finke, J. D., Buson, S., & Ciprini, S. 2019, *A&A*, 627, A140, doi: [10.1051/0004-6361/201935461](https://doi.org/10.1051/0004-6361/201935461)
- Atwood, W. B., Abdo, A. A., Ackermann, M., et al. 2009, *ApJ*, 697, 1071, doi: [10.1088/0004-637X/697/2/1071](https://doi.org/10.1088/0004-637X/697/2/1071)
- Ballet, J., Bruel, P., Burnett, T. H., Lott, B., & collaboration, T. F.-L. 2024, *Fermi Large Area Telescope Fourth Source Catalog Data Release 4 (4FGL-DR4)*. <https://arxiv.org/abs/2307.12546>
- Blandford, R. D., & Rees, M. J. 1978, *PhysS*, 17, 265, doi: [10.1088/0031-8949/17/3/020](https://doi.org/10.1088/0031-8949/17/3/020)
- Błażejowski, M., Sikora, M., Moderski, R., & Madejski, G. M. 2000, *ApJ*, 545, 107, doi: [10.1086/317791](https://doi.org/10.1086/317791)
- Bloom, S. D., & Marscher, A. P. 1996, *ApJ*, 461, 657, doi: [10.1086/177092](https://doi.org/10.1086/177092)
- Böttcher, M., & Els, P. 2016, *ApJ*, 821, 102, doi: [10.3847/0004-637X/821/2/102](https://doi.org/10.3847/0004-637X/821/2/102)
- Böttcher, M., Reimer, A., Sweeney, K., & Prakash, A. 2013, *ApJ*, 768, 54, doi: [10.1088/0004-637X/768/1/54](https://doi.org/10.1088/0004-637X/768/1/54)



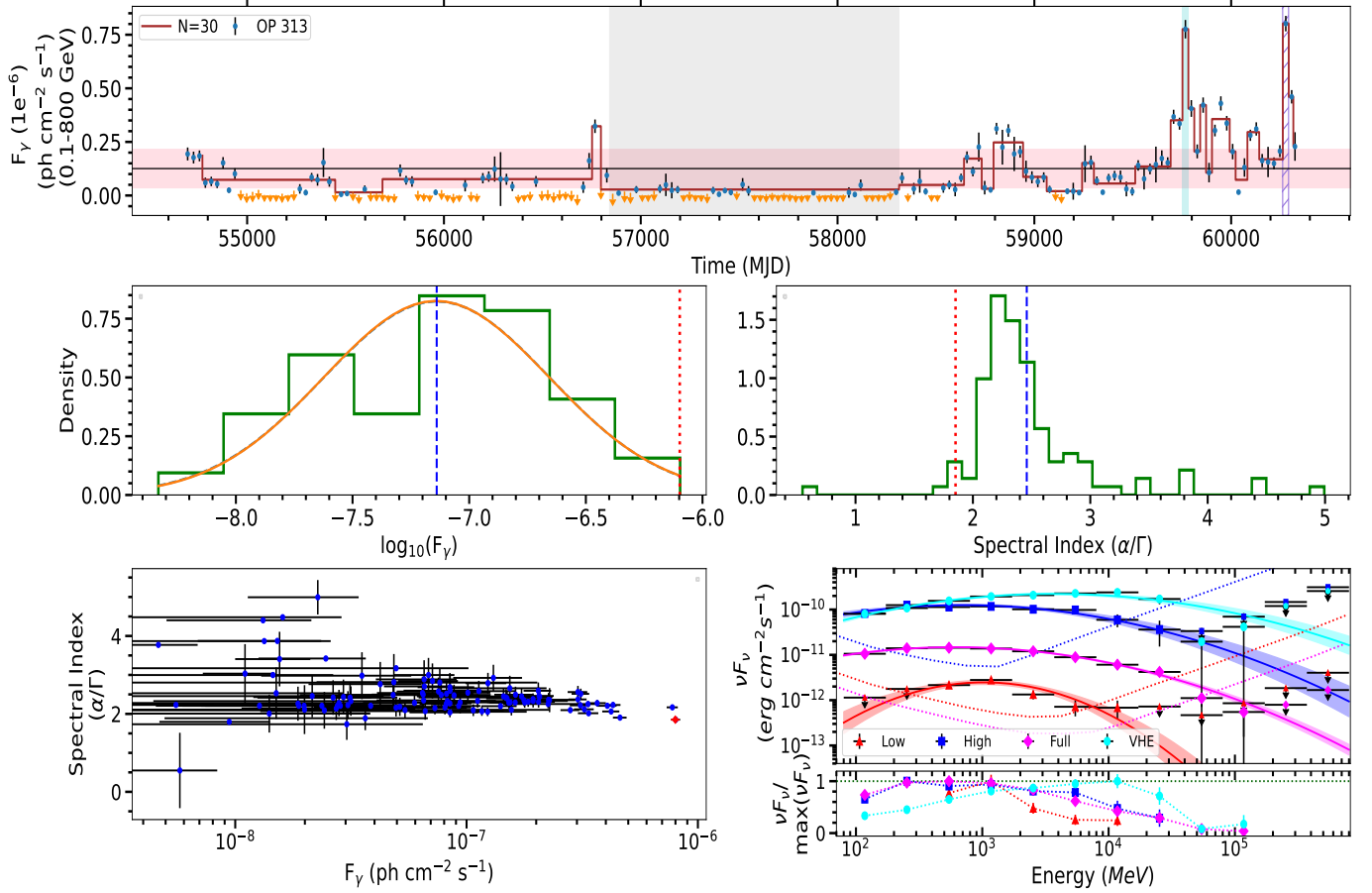


**Figure 6.** Top panel: Monthly binned lightcurve for the 10th VHE FSRQ OP 313. Middle panel: Histogram of logarithmic flux (left) and histogram of spectral index (right). Bottom panel: Spectral index versus photon flux (left) and MeV-GeV SED during low (Low) and high (High) flux states, along with the SED for the entire observation period (Full) and VHE detected durations (VHE; left). The other details are the same as in Figures 1, 2, 3 & 4.

Burbidge, E. M., & Rosenberg, F. D. 1965, *ApJ*, 142, 1673, doi: [10.1086/148458](https://doi.org/10.1086/148458)

Cerruti, M. 2015, arXiv e-prints, arXiv:1501.03554, doi: [10.48550/arXiv.1501.03554](https://doi.org/10.48550/arXiv.1501.03554)

Cohen, J. G., Lawrence, C. R., & Blandford, R. D. 2003, *ApJ*, 583, 67, doi: [10.1086/344837](https://doi.org/10.1086/344837)

Costamante, L., Cutini, S., Tosti, G., Antolini, E., & Tramacere, A. 2018, *MNRAS*, 477, 4749, doi: [10.1093/mnras/sty887](https://doi.org/10.1093/mnras/sty887)

Dathan, L., & Kushwaha, P. 2025, arXiv e-prints, arXiv:2504.05083, doi: [10.48550/arXiv.2504.05083](https://doi.org/10.48550/arXiv.2504.05083)

Dermer, C. D., & Schlickeiser, R. 1992, *Science*, 257, 1642, doi: [10.1126/science.257.5077.1642](https://doi.org/10.1126/science.257.5077.1642)

Fan, J. H., Yuan, Y.-H., Liu, Y., et al. 2008, *Publications of The Astronomical Society of Japan - PUBL ASTRON SOC JPN*, 60, doi: [10.1093/pasj/60.4.707](https://doi.org/10.1093/pasj/60.4.707)

Fossati, G., Maraschi, L., Celotti, A., Comastri, A., & Ghisellini, G. 1998, *MNRAS*, 299, 433, doi: [10.1046/j.1365-8711.1998.01828.x](https://doi.org/10.1046/j.1365-8711.1998.01828.x)

Gao, S., Fedynitch, A., Winter, W., & Pohl, M. 2019, *Nature Astronomy*, 3, 88, doi: [10.1038/s41550-018-0610-1](https://doi.org/10.1038/s41550-018-0610-1)

Ghisellini, G., Righi, C., Costamante, L., & Tavecchio, F. 2017, *MNRAS*, 469, 255, doi: [10.1093/mnras/stx806](https://doi.org/10.1093/mnras/stx806)

Ghisellini, G., & Tavecchio, F. 2009, *MNRAS*, 397, 985, doi: [10.1111/j.1365-2966.2009.15007.x](https://doi.org/10.1111/j.1365-2966.2009.15007.x)

Gravity Collaboration, Sturm, E., Dexter, J., et al. 2018, *Nature*, 563, 657, doi: [10.1038/s41586-018-0731-9](https://doi.org/10.1038/s41586-018-0731-9)

H. E. S. S. Collaboration, Abramowski, A., Acero, F., et al. 2010, *A&A*, 520, A83, doi: [10.1051/0004-6361/201014484](https://doi.org/10.1051/0004-6361/201014484)

—. 2013, *A&A*, 554, A107, doi: [10.1051/0004-6361/201321135](https://doi.org/10.1051/0004-6361/201321135)

H. E. S. S. Collaboration, Abdalla, H., Adam, R., et al. 2019, *A&A*, 627, A159, doi: [10.1051/0004-6361/201935704](https://doi.org/10.1051/0004-6361/201935704)

—. 2020, *A&A*, 633, A162, doi: [10.1051/0004-6361/201935906](https://doi.org/10.1051/0004-6361/201935906)

Hayashida, M., Nalewajko, K., Madejski, G. M., et al. 2015, *ApJ*, 807, 79, doi: [10.1088/0004-637X/807/1/79](https://doi.org/10.1088/0004-637X/807/1/79)



- Hewett, P. C., & Wild, V. 2010, *MNRAS*, 405, 2302, doi: [10.1111/j.1365-2966.2010.16648.x](https://doi.org/10.1111/j.1365-2966.2010.16648.x)
- Ho, L. C., & Kim, M. 2009, *ApJS*, 184, 398, doi: [10.1088/0067-0049/184/2/398](https://doi.org/10.1088/0067-0049/184/2/398)
- Itoh, R., Nalewajko, K., Fukazawa, Y., et al. 2016, *ApJ*, 833, 77, doi: [10.3847/1538-4357/833/1/77](https://doi.org/10.3847/1538-4357/833/1/77)
- Jaffe, W., Meisenheimer, K., Röttgering, H. J. A., et al. 2004, *Nature*, 429, 47, doi: [10.1038/nature02531](https://doi.org/10.1038/nature02531)
- Knuth, K. H. 2013, Optimal Data-Based Binning for Histograms. <https://arxiv.org/abs/physics/0605197>
- Kushwaha, P. 2025, *Universe*, 11, doi: [10.3390/universe11030084](https://doi.org/10.3390/universe11030084)
- Kushwaha, P., Chandra, S., Misra, R., et al. 2016, *ApJL*, 822, L13, doi: [10.3847/2041-8205/822/1/L13](https://doi.org/10.3847/2041-8205/822/1/L13)
- Kushwaha, P., Pal, M., Kalita, N., et al. 2021, *ApJ*, 921, 18, doi: [10.3847/1538-4357/ac19b8](https://doi.org/10.3847/1538-4357/ac19b8)
- Kushwaha, P., Sinha, A., Misra, R., Singh, K. P., & de Gouveia Dal Pino, E. M. 2017, *ApJ*, 849, 138, doi: [10.3847/1538-4357/aa8ef5](https://doi.org/10.3847/1538-4357/aa8ef5)
- Kushwaha, P., Gupta, A. C., Wiita, P. J., et al. 2018, *MNRAS*, 479, 1672, doi: [10.1093/mnras/sty1499](https://doi.org/10.1093/mnras/sty1499)
- Lioudakis, I., & Petropoulou, M. 2020, *ApJL*, 893, L20, doi: [10.3847/2041-8213/ab830a](https://doi.org/10.3847/2041-8213/ab830a)
- MAGIC Collaboration, Acciari, V. A., Ansoldi, S., et al. 2018, *A&A*, 619, A159, doi: [10.1051/0004-6361/201833618](https://doi.org/10.1051/0004-6361/201833618)
- . 2021, *A&A*, 647, A163, doi: [10.1051/0004-6361/202039687](https://doi.org/10.1051/0004-6361/202039687)
- Malik, Z., Akbar, S., Shah, Z., et al. 2025, *MNRAS*, 539, 2185, doi: [10.1093/mnras/staf620](https://doi.org/10.1093/mnras/staf620)
- Malmrose, M. P., Marscher, A. P., Jorstad, S. G., Nikutta, R., & Elitzur, M. 2011, *ApJ*, 732, 116, doi: [10.1088/0004-637X/732/2/116](https://doi.org/10.1088/0004-637X/732/2/116)
- Mannheim, K., & Biermann, P. L. 1992, *A&A*, 253, L21
- Manzoor, A., Shah, Z., Sahayanathan, S., Iqbal, N., & Dar, A. A. 2024, *MNRAS*, 529, 1356, doi: [10.1093/mnras/stae588](https://doi.org/10.1093/mnras/stae588)
- Maraschi, L., Ghisellini, G., & Celotti, A. 1992, *ApJL*, 397, L5, doi: [10.1086/186531](https://doi.org/10.1086/186531)
- Maurya, S., Majumdar, J., Varun, Sahu, N., & Prince, R. 2025, *PASA*, 42, e053, doi: [10.1017/pasa.2025.34](https://doi.org/10.1017/pasa.2025.34)
- Meyer, E. T., & Georganopoulos, M. 2014, *ApJL*, 780, L27, doi: [10.1088/2041-8205/780/2/L27](https://doi.org/10.1088/2041-8205/780/2/L27)
- Meyer, M., Scargle, J. D., & Blandford, R. D. 2019, *ApJ*, 877, 39, doi: [10.3847/1538-4357/ab1651](https://doi.org/10.3847/1538-4357/ab1651)
- Middei, R., Lioudakis, I., Perri, M., et al. 2023, *ApJL*, 942, L10, doi: [10.3847/2041-8213/aca281](https://doi.org/10.3847/2041-8213/aca281)
- Mirzoyan, R. 2017, *The Astronomer's Telegram*, 11061, 1
- Mücke, A., & Protheroe, R. J. 2001, *Astroparticle Physics*, 15, 121, doi: [10.1016/S0927-6505\(00\)00141-9](https://doi.org/10.1016/S0927-6505(00)00141-9)
- Nievas Rosillo, M., Acero, F., Otero-Santos, J., et al. 2024, arXiv e-prints, arXiv:2409.20487, doi: [10.48550/arXiv.2409.20487](https://doi.org/10.48550/arXiv.2409.20487)
- Osterbrock, D. E., & Pogge, R. W. 1987, *ApJ*, 323, 108, doi: [10.1086/165810](https://doi.org/10.1086/165810)
- Pandey, A., Kushwaha, P., Wiita, P. J., et al. 2024, *A&A*, 681, A116, doi: [10.1051/0004-6361/202347719](https://doi.org/10.1051/0004-6361/202347719)
- Pian, E., Vacanti, G., Tagliaferri, G., et al. 1998, *ApJL*, 492, L17, doi: [10.1086/311083](https://doi.org/10.1086/311083)
- Roy, A., Patel, S. R., Sarkar, A., Chatterjee, A., & Chitnis, V. R. 2021, *MNRAS*, 504, 1103, doi: [10.1093/mnras/stab975](https://doi.org/10.1093/mnras/stab975)
- Sahayanathan, S., & Godambe, S. 2012, *MNRAS*, 419, 1660, doi: [10.1111/j.1365-2966.2011.19829.x](https://doi.org/10.1111/j.1365-2966.2011.19829.x)
- Scargle, J. D., Norris, J. P., Jackson, B., & Chiang, J. 2013, *ApJ*, 764, 167, doi: [10.1088/0004-637X/764/2/167](https://doi.org/10.1088/0004-637X/764/2/167)
- Schneider, D. P., Richards, G. T., Hall, P. B., et al. 2010, *AJ*, 139, 2360, doi: [10.1088/0004-6256/139/6/2360](https://doi.org/10.1088/0004-6256/139/6/2360)
- Shah, Z., Mankuzhiyil, N., Sinha, A., et al. 2018, *Research in Astronomy and Astrophysics*, 18, 141, doi: [10.1088/1674-4527/18/11/141](https://doi.org/10.1088/1674-4527/18/11/141)
- Shaw, M. S., Romani, R. W., Cotter, G., et al. 2012, *ApJ*, 748, 49, doi: [10.1088/0004-637X/748/1/49](https://doi.org/10.1088/0004-637X/748/1/49)
- Sikora, M., Begelman, M. C., & Rees, M. J. 1994, *ApJ*, 421, 153, doi: [10.1086/173633](https://doi.org/10.1086/173633)
- Tanner, A. M., Bechtold, J., Walker, C. E., Black, J. H., & Cutri, R. M. 1996, *AJ*, 112, 62, doi: [10.1086/117988](https://doi.org/10.1086/117988)
- Tavecchio, F., Maraschi, L., Sambruna, R. M., & Urry, C. M. 2000, *ApJL*, 544, L23, doi: [10.1086/317292](https://doi.org/10.1086/317292)
- Urry, C. M., & Padovani, P. 1995, *PASP*, 107, 803, doi: [10.1086/133630](https://doi.org/10.1086/133630)
- Valverde, J., Horan, D., Bernard, D., et al. 2020, *ApJ*, 891, 170, doi: [10.3847/1538-4357/ab765d](https://doi.org/10.3847/1538-4357/ab765d)
- Wagner, S., Rani, B., & H. E. S. S. Collaboration. 2021, *The Astronomer's Telegram*, 15020, 1
- Wagner, S. J., & Witzel, A. 1995, *Annual Review of Astronomy and Astrophysics*, 33, 163, doi: <https://doi.org/10.1146/annurev.aa.33.090195.001115>
- Wang, N., Yi, T.-F., Wang, L., et al. 2023, *Research in Astronomy and Astrophysics*, 23, 115011, doi: [10.1088/1674-4527/ace9b1](https://doi.org/10.1088/1674-4527/ace9b1)
- White, G. L., Jauncey, D. L., Savage, A., et al. 1988, *ApJ*, 327, 561, doi: [10.1086/166216](https://doi.org/10.1086/166216)
- Yadav, S., & Kushwaha, P. 2024, *Galaxies*, 12, 34, doi: [10.3390/galaxies12040034](https://doi.org/10.3390/galaxies12040034)
- Zacharias, M., Sitarek, J., Dominis Prester, D., et al. 2017, in *International Cosmic Ray Conference*, Vol. 301, 35th International Cosmic Ray Conference (ICRC2017), 655, doi: [10.22323/1.301.0655](https://doi.org/10.22323/1.301.0655)